Proceedings of the IEOM International Conference on Smart Mobility and Vehicle Electrification
Detroit, Michigan, USA, October 10-12, 2023

Development of Electric Vehicle Simulation Model with DC BUS V/I-dependent Efficiency Map for Si IGBT and SiC MOSFET-based Traction Inverters

Kenton Kyger, Allan R. Taylor, and Chen Duan*
Electrical and Computer Engineering Department
Kettering University
Flint, Michigan 48504, USA
kyge7968@kettering.edu, ataylor@kettering.edu, cduan@kettering.edu

Abstract

In the realm of electrified vehicle development, vehicle simulations employing drive cycle inputs typically span thousands of seconds. Within this time domain, executing inverter motor control simulations with step sizes smaller than 1ms is not practical. To address this challenge, this research proposes a method of modeling electrified vehicles using an inverter efficiency map predicated on DC bus voltage and current. Theoretical analyses have corroborated that pivotal factors—such as collector voltage and current for Insulated-Gate Bipolar Transistors (IGBT) and Metal-Oxide-Semiconductor Field-Effect Transistors (MOSFET)—are dictated by the DC bus voltage and current, provided that the switching frequency and modulation index are fixed. Hence, power electronics simulations of inverters can be conducted at varying DC bus voltages and currents to create efficiency maps for prospective semiconductors. Tests have been performed on the Silicon IGBT IKW50N60DTP and Silicon Carbide MOSFET C3M0015065K. With the inclusion of the developed efficiency maps, a Tesla Model S vehicle model has been constructed and simulated. The simulation results from the combined Urban Dynamometer Driving Schedule (UDDS) and Highway Fuel Economy Test (HFET) drive cycle confirm that the SiC MOSFET-based inverter boasts greater and more consistent efficiency than its Si IGBT counterpart.

Keywords
Electric vehicle, Simulation, Inverter, SiC MOSFET, IGBT.

1. Introduction
Simulation based on test data is frequently employed for tasks such as component sizing, range prediction, and other performance estimations in the development of electrified vehicles (Powell et al. 1998). However, when it comes to evaluating a candidate system for which some test data—such as efficiency—is unavailable, executing an accurate simulation can be challenging.

Traction inverters serve as a prime example of these challenges. The switching frequency of inverter semiconductors is at the kHz level, necessitating a simulation step size of less than 1ms. However, performing simulations at this level of granularity for vehicle-level applications is not feasible, considering that a drive cycle can span thousands of seconds. Thus, there is a clear need for more adaptable and scalable simulation methods in the field of electrified vehicle development. In a previous study, Zhu et al. (2018) introduced a method that interpolates vehicle operating conditions at the inverter's switching period resolution. However, this approach necessitates repetitive work across various drive cycles, and experimental testing is still indispensable. In another study, a component loss map was generated from test data and integrated into the vehicle model to calculate efficiency (Su et al. 2019). While this method provides useful insights, it requires the acquisition of substantial test data, which can prove challenging when assessing multiple candidate semiconductor devices. Therefore, both approaches underscore the need for efficient methodologies that can navigate these complexities in the field of electrified vehicle development.

In this paper, we propose a method to estimate the power loss of a traction inverter using DC bus voltage and current. Based on our proof that the power loss of a traction inverter is determined by the DC bus voltage and current, we conduct a component-level simulation to estimate power loss at each operating point. This simulation can be performed in software such as PSpice, which utilizes a real component library, ensuring high accuracy in our results.

1.1 IGBT Power Loss

Miao et al. (2018) postulate that IGBT conduction loss can be represented as

$$P_{cond_{IGBT}} = \frac{1}{2}\left(V_{CEO} \cdot \frac{I_{ac}}{\pi} + r_C \cdot \frac{{I_{ac}}^2}{4}\right) + m \cdot \cos\varphi \cdot \left(V_{CEO} \cdot \frac{I_{ac}}{8} + r_C \cdot \frac{{I_{ac}}^2}{3\pi}\right) \quad (1)$$

Where V_{CEO} represents the threshold voltage drop of the IGBT, r_C represents the conduction resistance of the IGBT, and $\cos\varphi$ represents the power factor of the inverter with a phase shift angle of φ between output voltage and current. These contributors are treated as constants when the inverter remains at a single operating point. The three-phase SPWM modulation factor m is equivalent to

$$m = \frac{2\sqrt{6} \cdot V_{ac,rms}}{3 \cdot V_{dc}} \quad (2)$$

Where $V_{ac,rms}$ is the RMS AC line output voltage and V_{dc} is the input DC voltage. $V_{ac,rms}$ is typically a fixed value. I_{ac} in (1) represents the amplitude of AC current output. The RMS AC current output $I_{ac,rms}$ is obtained from I_{ac} via

$$I_{ac,rms} = \frac{I_{ac}}{\sqrt{2}} \quad (3)$$

For simulation, lossless operation is initially assumed to obtain operating setpoint conditions, then the losses from the obtained operating conditions are computed. Given the lossless operation assumption, AC voltage and current can be related to DC voltage and current via

$$P = V_{dc} \cdot I_{dc} = \sqrt{3} \cdot V_{ac,rms} \cdot I_{ac,rms} \cdot \cos\varphi = \sqrt{3} \cdot V_{ac,rms} \cdot \frac{I_{ac}}{\sqrt{2}} \cdot \cos\varphi \quad (4)$$

I_{ac}, then, is equivalent to

$$I_{ac} = \frac{\sqrt{2} \cdot V_{dc} \cdot I_{dc}}{\sqrt{3} \cdot V_{ac,rms} \cdot \cos\varphi} \quad (5)$$

Substituting (2) and (5) into (1), $P_{cond_{IGBT}}$ can be represented as

$$P_{cond_{IGBT}} = \frac{1}{2}\left(V_{CEO} \cdot \frac{\frac{\sqrt{2} \cdot V_{dc} \cdot I_{dc}}{\sqrt{3} \cdot V_{ac,rms} \cdot \cos\varphi}}{\pi} + r_C \cdot \frac{\left(\frac{\sqrt{2} \cdot V_{dc} \cdot I_{dc}}{\sqrt{3} \cdot V_{ac,rms} \cdot \cos\varphi}\right)^2}{4}\right) + \frac{2\sqrt{6} \cdot V_{ac,rms}}{3 \cdot V_{dc}} \cdot \cos\varphi \cdot \left(V_{CEO} \cdot \frac{\frac{\sqrt{2} \cdot V_{dc} \cdot I_{dc}}{\sqrt{3} \cdot V_{ac,rms} \cdot \cos\varphi}}{8} + r_C \cdot \frac{\left(\frac{\sqrt{2} \cdot V_{dc} \cdot I_{dc}}{\sqrt{3} \cdot V_{ac,rms} \cdot \cos\varphi}\right)^2}{3\pi}\right) \quad (6)$$

Which simplifies to

$$P_{cond_{IGBT}} = \frac{4\sqrt{6} \cdot {I_{dc}}^2 \cdot V_{dc} \cdot r_C}{27\pi \cdot V_{ac,rms} \cdot \cos\varphi} + \frac{{I_{dc}}^2 \cdot {V_{dc}}^2 \cdot r_C}{12 \cdot {V_{ac,rms}}^2 \cdot \cos^2\varphi} + \frac{I_{dc} \cdot V_{CEO}}{6} + \frac{\sqrt{6} \cdot I_{dc} \cdot V_{dc} \cdot V_{CEO}}{6\pi \cdot V_{ac,rms} \cdot \cos\varphi} \quad (7)$$

Switching loss in the IGBT occurs in the transient state between conduction and cutoff. Miao et al. (2018) state that IGBT switching loss can be represented as

$$P_{SW_{Tr}} = f_{SW}\left(E_{on} + E_{off}\right) \cdot \frac{V_{dc}}{V_N} \cdot \frac{I_{dc}}{I_N} \cdot \left[1 + k_{E_{Tr}}\left(125 - T_{j_{Tr}}\right)\right] \quad (8)$$

Where f_{SW} is the switching frequency, E_{on} represents the losses of conduction under rated conditions of the IGBT, and E_{off} represents the losses of cutoff under rated conditions of the IGBT. V_N and I_N are the nominal input DC voltage and DC current to the IGBT under rated conditions. V_{dc} and I_{dc} are the "actual" input DC voltage and DC current to the IGBT, and $T_{j_{Tr}}$ is the IGBT junction temperature at the selected operating point. The losses under rated conditions are temperature-compensated via an experimentally derived correction coefficient $k_{E_{Tr}}$ to adjust to the selected inverter operating point. f_{SW}, E_{on}, E_{off}, V_N, I_N, $k_{E_{Tr}}$, and $T_{j_{Tr}}$ remain constant while the inverter is operated at a given operating condition. Therefore, $P_{SW_{Tr}}$ is expressed as a function of I_{dc} and V_{dc}.

The total power loss of the IGBT is

$$P_{Tr} = P_{cond_{IGBT}} + P_{SW_{Tr}} \tag{9}$$

Substituting (7) and (8) into (9) yields

$$\begin{aligned} P_{Tr} = {} & \frac{4\sqrt{6} \cdot {I_{dc}}^2 \cdot V_{dc} \cdot r_C}{27\pi \cdot V_{ac,rms} \cdot \cos\varphi} + \frac{{I_{dc}}^2 \cdot {V_{dc}}^2 \cdot r_C}{12 \cdot {V_{ac,rms}}^2 \cdot \cos^2\varphi} + \frac{I_{dc} \cdot V_{CEO}}{6} + \frac{\sqrt{6} \cdot I_{dc} \cdot V_{dc} \cdot V_{CEO}}{6\pi \cdot V_{ac,rms} \cdot \cos\varphi} \\ & + f_{SW}\left(E_{on} + E_{off}\right) \cdot \frac{V_{dc}}{V_N} \cdot \frac{I_{dc}}{I_N} \cdot \left[1 + k_{E_{Tr}}\left(125 - T_{j_{Tr}}\right)\right] \end{aligned} \tag{10}$$

This derivation demonstrates that, for any given operating point of the IGBT-based inverter, P_{Tr} is a function of I_{dc} and V_{dc} as all other terms are constant.

Miao et al. (2018) state that diode conduction loss can be represented as

$$P_{cond_D} = \frac{1}{2}\left(V_{TO} \cdot \frac{I_{ac}}{\pi} + r_T \cdot \frac{{I_{ac}}^2}{4}\right) + m \cdot \cos\varphi \cdot \left(V_{TO} \cdot \frac{I_{ac}}{8} + r_T \cdot \frac{{I_{ac}}^2}{3\pi}\right) \tag{11}$$

Where V_{TO} is the threshold voltage drop of the diode and r_T is the conduction resistance of the diode, both of which are constants for a given inverter operating setpoint. Substituting (2) and (5) into (11), P_{cond_D} can also be represented as

$$\begin{aligned} P_{cond_D} = {} & \frac{1}{2}\left(V_{TO} \cdot \frac{\frac{\sqrt{2} \cdot V_{dc} \cdot I_{dc}}{\sqrt{3} \cdot V_{ac,rms} \cdot \cos\varphi}}{\pi} + r_T \cdot \frac{\left(\frac{\sqrt{2} \cdot V_{dc} \cdot I_{dc}}{\sqrt{3} \cdot V_{ac,rms} \cdot \cos\varphi}\right)^2}{4}\right) + \frac{2\sqrt{6} \cdot V_{ac,rms}}{3 \cdot V_{dc}} \cdot \cos\varphi \\ & \cdot \left(V_{TO} \cdot \frac{\frac{\sqrt{2} \cdot V_{dc} \cdot I_{dc}}{\sqrt{3} \cdot V_{ac,rms} \cdot \cos\varphi}}{8} + r_T \cdot \frac{\left(\frac{\sqrt{2} \cdot V_{dc} \cdot I_{dc}}{\sqrt{3} \cdot V_{ac,rms} \cdot \cos\varphi}\right)^2}{3\pi}\right) \end{aligned} \tag{12}$$

Which simplifies to

$$P_{cond_D} = \frac{4\sqrt{6} \cdot {I_{dc}}^2 \cdot V_{dc} \cdot r_T}{27\pi \cdot V_{ac,rms} \cdot \cos\varphi} + \frac{{I_{dc}}^2 \cdot {V_{dc}}^2 \cdot r_T}{12 \cdot {V_{ac,rms}}^2 \cdot \cos^2\varphi} + \frac{I_{dc} \cdot V_{TO}}{6} + \frac{\sqrt{6} \cdot I_{dc} \cdot V_{dc} \cdot V_{TO}}{6\pi \cdot V_{ac,rms} \cdot \cos\varphi} \tag{13}$$

Miao et al. (2018) state that diode switching loss, which occurs in the transient state between cutoff and conduction, can be represented as

$$P_{SW_D} = f_{SW} \cdot E_{rec} \cdot \frac{V_{dc}}{V_N} \cdot \frac{I_{dc}}{I_N} \cdot \left[1 + k_{E_D}\left(125 - T_{j_D}\right)\right] \tag{14}$$

Where E_{rec} represents the reverse-recovery ("switching") loss of the diode under the rated conditions and T_{j_D} represents the diode junction temperature. The losses under rated conditions are temperature-compensated via an experimentally derived correction coefficient k_{E_D} to adjust to the selected inverter operating point. f_{SW}, E_{rec}, V_N, I_N, k_{E_D}, and T_{j_D} remain constant while the inverter is operated at a given operating condition. Therefore, P_{SW_D} is expressed as a function of I_{dc} and V_{dc}.

The total diode power loss is

$$P_D = P_{cond_D} + P_{SW_D} \tag{15}$$

Substituting (12) and (13) into (14) yields

$$\begin{aligned} P_D = {} & \frac{4\sqrt{6} \cdot {I_{dc}}^2 \cdot V_{dc} \cdot r_T}{27\pi \cdot V_{ac,rms} \cdot \cos\varphi} + \frac{{I_{dc}}^2 \cdot {V_{dc}}^2 \cdot r_T}{12 \cdot {V_{ac,rms}}^2 \cdot \cos^2\varphi} + \frac{I_{dc} \cdot V_{TO}}{6} + \frac{\sqrt{6} \cdot I_{dc} \cdot V_{dc} \cdot V_{TO}}{6\pi \cdot V_{ac,rms} \cdot \cos\varphi} + f_{SW} \cdot E_{rec} \cdot \frac{V_{dc}}{V_N} \\ & \cdot \frac{I_{dc}}{I_N} \cdot \left[1 + k_{E_D}\left(125 - T_{j_D}\right)\right] \end{aligned} \tag{16}$$

This derivation demonstrates that, for any given operating point of the IGBT-based inverter, P_D is a function of I_{dc} and V_{dc} as all other terms are constant.

1.2 SiC MOSFET Power Loss

Gurpinar and Ozpineci (2018) indicate that SiC MOSFET forward conduction loss can be represented as

$$P_{cond_M} = P_{cond_+} + P_{cond_-} + P_{dt_1} + P_{dt_2} - P_{dt_{red}} \tag{17}$$

Where P_{cond_+} is conduction loss in the positive state, P_{cond_-} is conduction loss in the negative state, P_{dt_1} is the dead-time conduction loss in the 0 to φ region, P_{dt_2} is the dead-time conduction loss in the φ to π region, and $P_{dt_{red}}$ is the reduction in conduction loss due to dead-time duration reducing the total conduction time. P_{cond_+} and P_{cond_-} can be expressed as

$$P_{cond_+} + P_{cond_-} = \frac{r_{DS} \cdot {I_{ac,rms}}^2}{8} \tag{18}$$

Where r_{DS} is the on-state switch resistance. P_{dt_1} can be expressed as

$$P_{dt_1} = \frac{t_{dt} \cdot f_{SW}}{\pi}\left[V_{th} \cdot \frac{I_{ac}}{2}(1 - \cos(-\varphi)) + \frac{{I_{ac}}^2}{4} \cdot r_{SD}\left(\frac{\varphi}{2} - \frac{\sin(2\varphi)}{4}\right)\right] \tag{19}$$

Where t_{dt} is the dead-time duration, V_{th} is on-state threshold voltage of the body diode, and r_{SD} is on-state resistance of the body diode. P_{dt_2} can be expressed as

$$P_{dt_2} = \frac{t_{dt} \cdot f_{SW}}{\pi}\left[V_{th} \cdot \frac{I_{ac}}{2} \cdot (\cos(\pi - \varphi) - 1) + \frac{{I_{ac}}^2}{4} \cdot r_{SD} \cdot \left(\frac{\pi - \varphi}{2} + \frac{\sin(2\varphi)}{4}\right)\right] \tag{20}$$

$P_{dt_{red}}$ can be expressed as

$$P_{dt_{red}} = \frac{t_{dt} \cdot f_{SW} \cdot r_{DS} \cdot {I_{ac}}^2}{8} \tag{21}$$

Substituting (5), (18), (19), (20), and (21) into (17) yields

$$\begin{aligned} P_{cond_M} = {} & \frac{r_{DS} \cdot \left(\frac{V_{dc} \cdot I_{dc}}{\sqrt{3} \cdot V_{ac,rms} \cdot \cos\varphi}\right)^2}{8} + \frac{t_{dt} \cdot f_{SW}}{\pi}\left[V_f \cdot \frac{\frac{\sqrt{2} \cdot V_{dc} \cdot I_{dc}}{\sqrt{3} \cdot V_{ac,rms} \cdot \cos\varphi}}{2}(1 - \cos(-\varphi))\right. \\ & \left. + \frac{\left(\frac{\sqrt{2} \cdot V_{dc} \cdot I_{dc}}{\sqrt{3} \cdot V_{ac,rms} \cdot \cos\varphi}\right)^2}{4} \cdot r_{SD}\left(\frac{\varphi}{2} - \frac{\sin(2\varphi)}{4}\right)\right] + \frac{t_{dt} \cdot f_{SW}}{\pi}\left[V_f \cdot \frac{\frac{\sqrt{2} \cdot V_{dc} \cdot I_{dc}}{\sqrt{3} \cdot V_{ac,rms} \cdot \cos\varphi}}{2}\right. \\ & \left. \cdot (\cos(\pi - \varphi) - 1) + \frac{\left(\frac{\sqrt{2} \cdot V_{dc} \cdot I_{dc}}{\sqrt{3} \cdot V_{ac,rms} \cdot \cos\varphi}\right)^2}{4} \cdot r_{SD} \cdot \left(\frac{\pi - \varphi}{2} + \frac{\sin(2\varphi)}{4}\right)\right] \\ & - \frac{t_{dt} \cdot f_{SW} \cdot r_{DS} \cdot \left(\frac{\sqrt{2} \cdot V_{dc} \cdot I_{dc}}{\sqrt{3} \cdot V_{ac,rms} \cdot \cos\varphi}\right)^2}{8} \end{aligned} \tag{22}$$

Which simplifies to

$$\begin{aligned} P_{cond_M} = {} & \frac{r_{DS} \cdot {V_{dc}}^2 \cdot {I_{dc}}^2}{24 \cdot {V_{ac,rms}}^2 \cdot \cos^2\varphi} - \frac{\sqrt{6} \cdot f_{SW} \cdot t_{dt} \cdot V_{th} \cdot V_{dc} \cdot I_{dc}}{3\pi \cdot V_{ac,rms}} + \frac{f_{SW} \cdot t_{dt} \cdot r_{SD} \cdot {V_{dc}}^2 \cdot {I_{dc}}^2}{12 \cdot {V_{ac,rms}}^2 \cdot \cos^2\varphi} \\ & - \frac{f_{SW} \cdot t_{dt} \cdot r_{DS} \cdot {V_{dc}}^2 \cdot {I_{dc}}^2}{12 \cdot {V_{ac,rms}}^2 \cdot \cos^2\varphi} \end{aligned} \tag{23}$$

This derivation demonstrates that, for any given operating point of the SiC MOSFET-based inverter, P_{cond_M} is a function of I_{dc} and V_{dc} as all other terms are constant.

Gurpinar and Ozpineci (2018) state that SiC MOSFET forward switching loss can be represented as

$$P_{SW_M} = P_{on} + P_{off} + P_{rr_D} \tag{24}$$

Where P_{on} is the turn-on switching loss, P_{off} is the turn-off switching loss, and P_{rr_D} is the reverse recovery loss across the body diode of the MOSFET. These three terms are assumed to be sufficient as SiC MOSFET datasheets typically incorporate the reverse recovery losses of the device under test into the turn-on loss data. Under the assumption that P_{on} and P_{off} change linearly with U_{dc} and i_{ds} for the SiC MOSFET C3M0015065K, P_{on} can be expressed as

$$P_{on} = \frac{f_{SW} \cdot I_{ac} \cdot V_{dc} \cdot E_{on,test}}{2\pi \cdot V_{DS,test} \cdot I_{DS,test}} \tag{25}$$

Where $E_{on,test}$ is turn-on switching loss energy, $I_{DS,test}$ is drain-source current, $V_{DS,test}$ is drain-source voltage, all of which are normalized to the inverter operating condition. Similarly, P_{off} can be expressed as

$$P_{off} = \frac{f_{SW} \cdot I_{ac} \cdot V_{dc} \cdot E_{off,test}}{2\pi \cdot V_{DS,test} \cdot I_{DS,test}} \tag{26}$$

Where $E_{on,test}$ is turn-off switching loss energy. P_{rr_D} can be expressed as

$$P_{rr_D} = \frac{f_{SW} \cdot t_b \cdot I_{RRM} \cdot V_{dc}}{12} \tag{27}$$

Where I_{RRM} is the peak reverse recovery of the SiC MOSFET diode and t_b is the time for I_{RRM} to decay to zero []. Substituting (5), (25), (26), and (27) into (24) yields

$$P_{SW_M} = \frac{f_{SW} \cdot \frac{\sqrt{2} \cdot V_{dc} \cdot I_{dc}}{\sqrt{3} \cdot V_{ac,rms} \cdot \cos\varphi} \cdot V_{dc} \cdot E_{on,test}}{2\pi \cdot V_{DS,test} \cdot I_{DS,test}} + \frac{f_{SW} \cdot \frac{\sqrt{2} \cdot V_{dc} \cdot I_{dc}}{\sqrt{3} \cdot V_{ac,rms} \cdot \cos\varphi} \cdot V_{dc} \cdot E_{off,test}}{2\pi \cdot V_{DS,test} \cdot I_{DS,test}} + \frac{f_{SW} \cdot t_b \cdot I_{RRM} \cdot V_{dc}}{12} \tag{28}$$

Which simplifies to

$$P_{SW_M} = \frac{\sqrt{6} \cdot f_{SW} \cdot E_{on,test} \cdot {V_{dc}}^2 \cdot I_{dc}}{6\pi \cdot V_{ac,rms} \cdot V_{DS,test} \cdot I_{DS,test} \cdot \cos\varphi} + \frac{\sqrt{6} \cdot f_{SW} \cdot E_{off,test} \cdot {V_{dc}}^2 \cdot I_{dc}}{6\pi \cdot V_{ac,rms} \cdot V_{DS,test} \cdot I_{DS,test} \cdot \cos\varphi} + \frac{f_{SW} \cdot t_b \cdot I_{RRM} \cdot V_{dc}}{12} \tag{29}$$

This derivation demonstrates that, for any given operating point of the SiC MOSFET-based inverter, P_{SW_M} is a function of I_{dc} and V_{dc} as all other terms are constant.

The total SiC MOSFET power loss is

$$P_M = P_{cond_M} + P_{SW_M} \tag{30}$$

Substituting (23) and (29) into (30) yields

$$P_M = \frac{r_{DS} \cdot {V_{dc}}^2 \cdot {I_{dc}}^2}{24 \cdot {V_{ac,rms}}^2 \cdot \cos^2\varphi} - \frac{\sqrt{6} \cdot f_{SW} \cdot t_{dt} \cdot V_{th} \cdot V_{dc} \cdot I_{dc}}{3\pi \cdot V_{ac,rms}} + \frac{f_{SW} \cdot t_{dt} \cdot r_{SD} \cdot {V_{dc}}^2 \cdot {I_{dc}}^2}{12 \cdot {V_{ac,rms}}^2 \cdot \cos^2\varphi} - \frac{f_{SW} \cdot t_{dt} \cdot r_{DS} \cdot {V_{dc}}^2 \cdot {I_{dc}}^2}{12 \cdot {V_{ac,rms}}^2 \cdot \cos^2\varphi} + \frac{\sqrt{6} \cdot f_{SW} \cdot E_{on,test} \cdot {V_{dc}}^2 \cdot I_{dc}}{6\pi \cdot V_{ac,rms} \cdot V_{DS,test} \cdot I_{DS,test} \cdot \cos\varphi} + \frac{\sqrt{6} \cdot f_{SW} \cdot E_{off,test} \cdot {V_{dc}}^2 \cdot I_{dc}}{6\pi \cdot V_{ac,rms} \cdot V_{DS,test} \cdot I_{DS,test} \cdot \cos\varphi} + \frac{f_{SW} \cdot t_b \cdot I_{RRM} \cdot V_{dc}}{12} \tag{31}$$

This derivation demonstrates that, for any given operating point of the SiC MOSFET-based inverter, P_M is a function of I_{dc} and V_{dc} as all other terms are constant.

2. Modeling Algorithm

The derivations in the previous section demonstrate that the traction inverter power loss can be estimated from DC bus voltage and current. Therefore, in a vehicle simulation model, power loss and efficiency of the traction inverter can be extracted from lookup tables instead of conducting a power electronics simulation at every single switching cycle. In this research, traction inverter efficiency maps were developed in PSpice with manufacturer semi-conductor models directly applied. To estimate power loss and efficiency of 2 switch candidates, Si IGBT IKW50N60DTP and SiC MOSFET C3M0015065K were utilized to develop 3-phase inverter models in PSpice with RL loads. For the SiC-based inverter, there are 4 MOSFETs in parallel on each arm; while for the IGBT-based counterpart, there are 3 switches in parallel. The switching frequencies were set to 50kHz for the SiC MOSFET-based inverter and 10kHz for the Si IGBT-based inverter, repectively. By changing the DC bus voltage and modulation index, efficiency lookup tables of the SiC MOSFET- and Si IGBT-based inverters vs. DC bus voltage and current were obtained, as shown in Figure 1 (a) and (b) respectively. The inverter efficiency maps were then embedded into the vehicle simulation model.

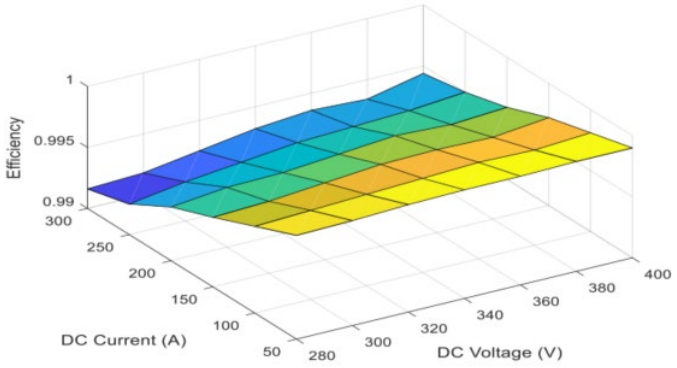

(a) SiC MOSFET-Based Inverter

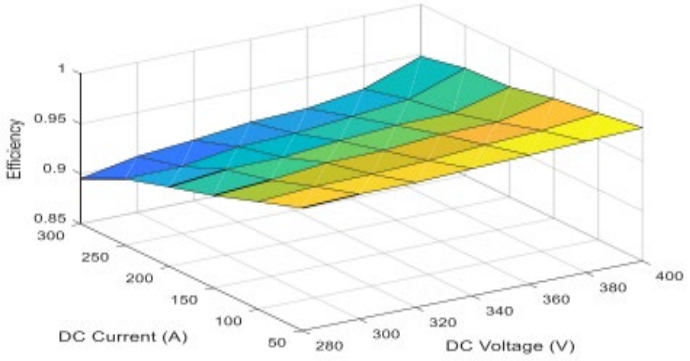

(b) Si IGBT-Based Inverter

Figure 1. Traction Inverter Efficiency vs. DC Bus Voltage and Current

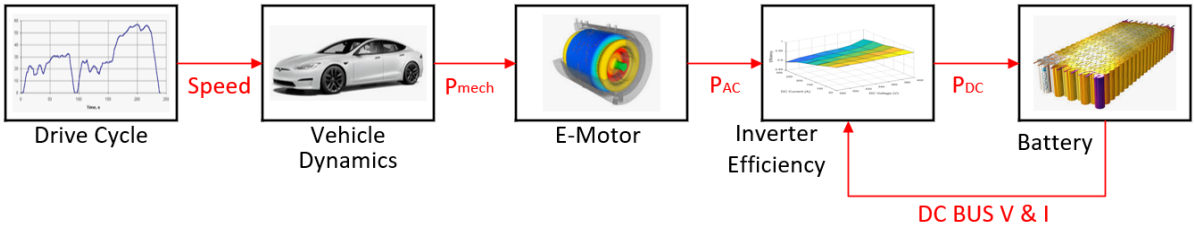

Figure 2. Backward Vehicle Simulation Architecture

The vehicle model was developed with backward architecture as shown in Figure 2. The vehicle dynamics block calculates the mechanical power that the e-motor needs to provide to overcome road load from the speed profile input. The e-motor block converts the mechanical power request to electric power (AC) request. The inverter block with embedded efficiency maps obtained from PSpice converts the power request from AC power to DC power, which charges/discharges the battery. Finally, the battery block estimates DC bus voltage and current to determine real-time inverter efficiency.

In the vehicle dynamics block, the mechanical power request is calculated as

$$P_{mech} = (k \cdot m \cdot a) + (F_{RL} \cdot v) \quad (32)$$

Where k is the mass factor to equivalent rotating parts inertia, m is the total weight of vehicle curb, driver and payload, a is the vehicle acceleration; F_{RL} is the road load force, and v is the vehicle speed. F_{RL} is calculated as

$$F_{RL} = F_{RR} + F_{AD} + F_{HC} \quad (33)$$

Where F_{RR} is the tire rolling resistance, F_{AD} is the air drag force, and F_{HC} is the hill climbing resistance. F_{RR} can be expressed as

$$F_{RR} = m \cdot g \cdot F_R \cdot \cos\theta \quad (34)$$

Where g is the acceleration due to gravity ($9.8\ N/kg$), F_R is the tire rolling friction coefficient, and θ is the road grade in degrees. F_{AD} from (33) can be expressed as

$$F_{AD} = 0.5 \cdot \rho_{air} \cdot A \cdot C_d \cdot v^2 \tag{35}$$

Where ρ_{air} is the air density, A is the vehicle frontal cross sectional area, and C_d is the air drag coefficient. F_{HC} is calculated as

$$F_{HC} = m \cdot g \cdot \sin\theta \tag{36}$$

The vehicle modeled in this research was a Tesla Model S with a single motor. The vehicle parameters are shown in Table 1 (Palin et al. 2012).

Table 1. Tesla Model S Single Motor Vehicle Parameters

Description	**Value**
Vehicle Curb Weight	2107kg
Driver and Load Weight	100kg
Vehicle Cross Section	3.4m^2
Tesla Drag Coefficient	0.208
Rolling Friction Coefficient	0.04
Mass Factor	1.1
Differential Gear Ratio Tire Radius	9.73 0.352m
Driveline Efficiency	98%

The e-motor block is modeled as an efficiency map from test data, shown in Figure 3 (Thomas et al. 2020). In this plot, positive torque indicates generated torque output and negative torque indicates regenerative braking torque.

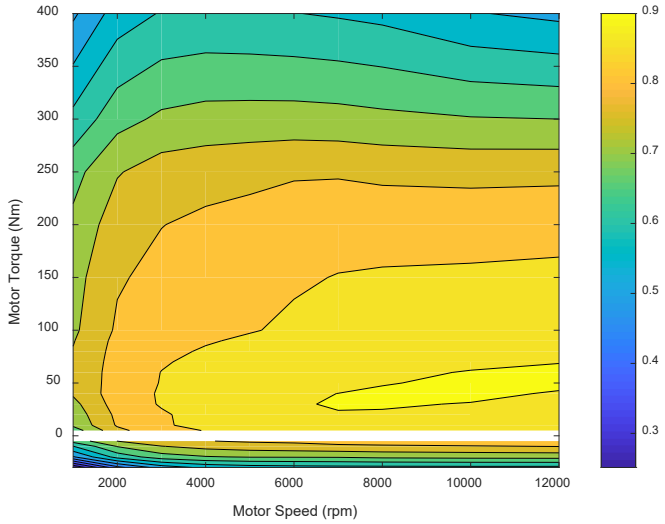

Figure 3. Motor Efficiency Map

The inverter block with embedded efficiency maps from PSpice converts AC power to DC power that charges/discharges the battery. The DC power is presented to the inverter block as

$$P_{dc} = \begin{cases} P_{mech} \div \eta_{mtr} \div \eta_{inv} \text{ if } P_{mech} > 0 \\ P_{mech} \cdot \eta_{mtr} \cdot \eta_{inv} \text{ if } P_{mech} < 0 \end{cases} \tag{37}$$

Where η_{mtr} and η_{inv} are motor and inverter efficiency, respectively. The battery block is formed by a state-of-charge (SOC) calculation module and a 2RC equivalent circuit model (Rajanma et al. 2020), as shown in Figure 4.

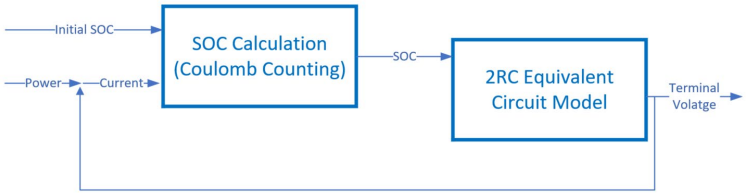

Figure 4. Battery Model Architecture

The SOC is estimated via the coulomb counting method, expressed as

$$SOC = SOC_{initial} - \frac{\int i_{dc}(t)dt}{C_{rate}} \tag{38}$$

Where $SOC_{initial}$ is the initial SOC, and C_{rate} is the rated battery capacity in Ah. The 2RC equivalent battery model is shown in Figure 5, in which the terminal voltage V_t is determined as

$$V_t = OCV - i_{dc}R_0 - \frac{1}{C_1}\int (i_{dc} - \frac{V_1}{R_1})dt - \frac{1}{C_2}\int (i_{dc} - \frac{V_2}{R_2})dt \tag{39}$$

Where OCV is the battery open circuit voltage, which is determined by the SOC. i_{dc} is he battery current calculated from DC power request and terminal voltage. V_1 and V_2 are the voltages of the first and second RC branch, respectively.

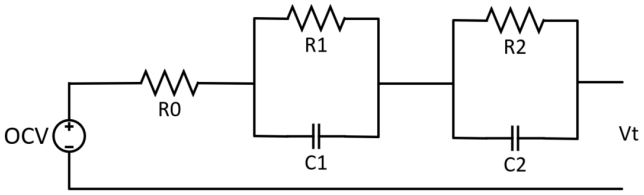

Figure 5. Battery Model Architecture

3. Simulation Results

Using the developed vehicle model, which includes an embedded inverter efficiency map, simulations have been performed for both Si IGBT- and SiC MOSFET-based traction inverters. A speed input profile that combines the Urban Dynamometer Driving Schedule (UDDS) and the Highway Fuel Economy Test (HFET) drive cycles was used, which is depicted in Figure 6. This combination allows for estimations under both urban and highway driving conditions. Figure 7 illustrates the simulated efficiency of the Si IGBT- and SiC MOSFET-based inverters, and Figure 8 highlights the power loss associated with each.

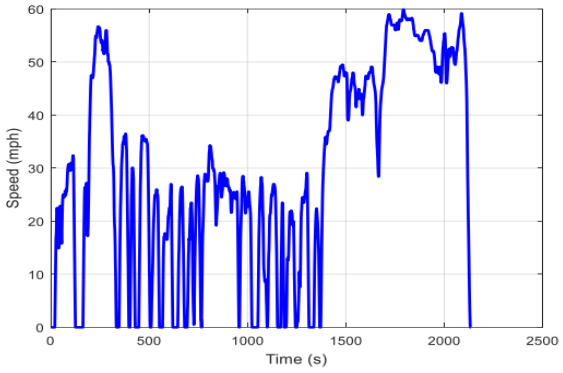

Figure 6. UDDS + HFET Drive Cycle

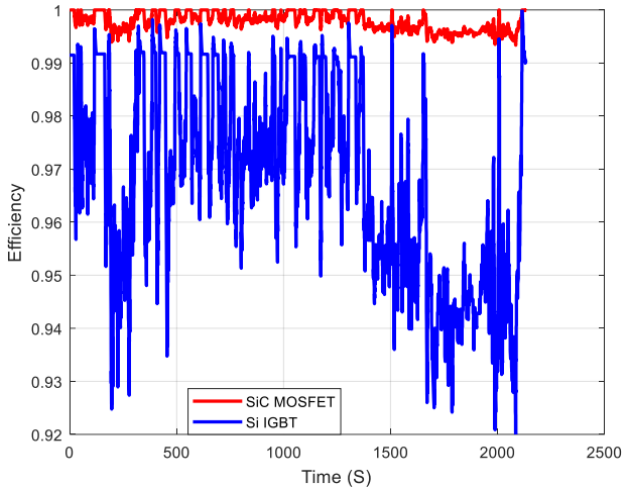

Figure 7. Inverter Efficiency of UDDS+HFET Cycle

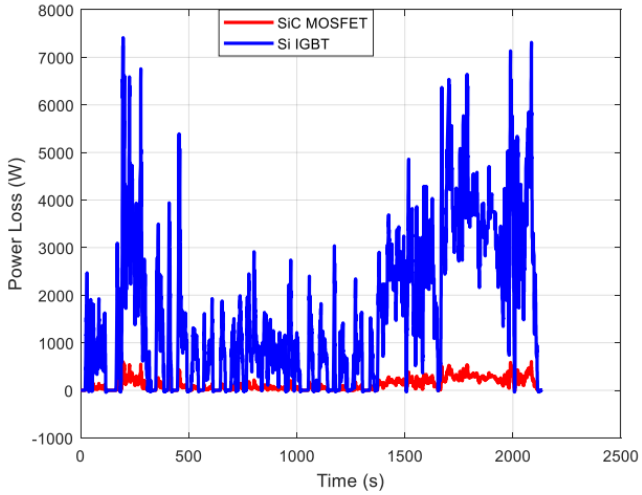

Figure 8. Inverter Power Loss of UDDS+HFET Cycle

Upon examining Figures 7 and 8, it is evident that the SiC MOSFET-based inverter exhibits higher and more stable efficiency than the Si IGBT-based inverter, translating to a significant reduction in power loss during the combined UDDS+HFET drive cycle. By integrating the power loss over this cycle, it was found that the total energy losses for SiC MOSFET- and Si IGBT-based inverters amount to 68.38Wh and 925.9Wh, respectively. This stark difference underscores the superior efficiency and lower energy loss characteristics of the SiC MOSFET-based inverter compared to its Si IGBT counterpart.

4. Conclusion

This research introduces a novel method for simulating electric vehicle inverter efficiency and estimating power loss. The method employs switch-cycle based simulation in PSpice to generate efficiency lookup tables corresponding to DC bus voltage and current of inverters with different semiconductors. A vehicle model with an embedded inverter efficiency map can be used to carry out simulations with durations in the thousands of seconds. The developed model, based on a Tesla Model S, has been tested with two candidate traction inverters, Si IGBT IKW50N60DTP and SiC MOSFET C3M0015065K, respectively. Simulation results confirm that SiC MOSFET proves to be a superior candidate compared to Si IGBT for traction inverter development. By adopting SiC MOSFET as the power switch, inverter efficiency can be maintained in the >99% range, saving 92.6% in energy loss.

References

Graovac, D. and Pürschel, M., *IGBT Power Losses Calculation Using the Data-Sheet Parameters*, Edition 2009-01-29, Infineon Technologies, 2009.

Gurpinar, E. and Ozpineci, B., Loss Analysis and Mapping of a SiC MOSFET Based Segmented Two-Level Three-Phase Inverter for EV Traction Systems, *2018 IEEE Transportation Electrification Conference and Expo (ITEC)*, pp. 1046-1053, Long Beach, CA, USA, June 13-15, 2018, doi: 10.1109/ITEC.2018.8450188.

Infineon Technologies, How to Select the Right CoolMOS and its Power Handling Capability, Available: https://www.infineon.com/dgdl/Infineon-ApplicationNote_MOSFET_CoolMOS_How_to_select_the_right_CoolMOS-AN-v01_00-EN.pdf?fileId=db3a304412b407950112b40acf580693, January, 2002.

Infineon Technologies, IKW50N60DTP, Accessible: https://www.infineon.com/dgdl/Infineon-IKW50N60DTP-DataSheet-v02_01-EN.pdf?fileId=5546d46253a864fe0153cbc2c1c17cc1, February, 2016.

Jiang, D., Burgos, R., Wang, F., and Boroyevich, D., Temperature-Dependent Characteristics of SiC Devices: Performance Evaluation and Loss Calculation, *IEEE Transactions on Power Electronics*, vol. 27, no. 2, pp. 1013-1024, 2012, doi: https://doi.org/10.1109/TPEL.2011.2159624.

Lakkas, G., MOSFET power losses and how they affect power-supply efficiency, Available: https://www.ti.com/lit/an/slyt664/slyt664.pdf, 2016.

Li, X., Zhang, L., Guo, S., Lei, Y., Huang, A., and B. Zhang, Understanding switching losses in SiC MOSFET: Toward lossless switching, *2015 IEEE 3rd Workshop on Wide Bandgap Power Devices and Applications (WiPDA)*, pp. 257-262, Blacksburg, VA, USA, November 02-04, 2015, doi: https://doi.org/10.1109/WiPDA.2015.7369295.

Miao, Y., Lei, W., Li, S., Lv, X., Li, B., Wang, P., Xu, J., and Li, H., Influence of Inverter DC Voltage on the Reliability of IGBT, *American Institute of Physics (AIP) Conference Proceedings*, pp. 020023-1-020023-8, Busan, South Korea, April 14-15, 2018, doi: https://doi.org/10.1063/1.5038995.

Palin, R., Johnston, V., Johnson, S., D'Hooge, A., Duncan, B., Gargoloff, J., The Aerodynamic Development of the Tesla Model S - Part 1: Overview, *SAE 2012 World Congress and Exhibition*, Detroit, MI, USA, April 24-26, 2012, doi: https://doi.org/10.4271/2012-01-0177.

Powell, B., Bailey, K., and Cikanek, S., Dynamic modeling and control of hybrid electric vehicle powertrain systems, *IEEE Control Systems Magazine*, vol.18, no. 5, pp.17-33, 1998.

Rajanna, B., and Malligunta K., Comparison of one and two time constant models for lithium ion battery, *International Journal of Electrical and Computer Engineering*, vol. 10, no. 1, pp. 670-680, 2020.

She, X., Huang, A., Lucía, Ó., and Ozpineci, B., Review of silicon carbide power devices and their applications, *IEEE Transactions on Industrial Electronics*, vol. 64, no. 10, pp. 8193–8205, 2017.

Su, M., Chen, C., Sharma, S., and Kikuchi., J., Performance and cost considerations for SiC-based HEV traction inverter systems. *2015 IEEE 3rd Workshop on Wide Bandgap Power Devices and Applications (WiPDA)*, pp. 347-350, Blacksburg, VA, USA, 2015.

Thomas, R,, Lauric G., Laurent G., and Hervé C., Modeling and design analysis of the Tesla Model S induction motor, *2020 IEEE International Conference on Electrical Machines (ICEM)*, pp. 495-501, Gothenburg, Sweden, 2020.

Wolfspeed, C3M0015065K, Accessible: https://assets.wolfspeed.com/uploads/2020/12/C3M0015065K.pdf, March, 2022.

Zhu, J., Kim, H., Chen, H., Erickson, R., and Maksimovic, D., High efficiency SiC traction inverter for electric vehicle applications, *2018 IEEE Applied Power Electronics Conference and Exposition (APEC)*, pp. 1428-1433, San Antonio, TX, USA, 2018.

Biographies

Kenton T. Kyger is a commercial valvetrain graduate co-op at the Eaton Corporation Proving Grounds in Marshall, MI and graduate student studying for an M.S.E. in Mobility Systems at Kettering University. He received his B.S. in Electrical Engineering and B.S. in Mechanical Engineering with an automotive design specialty from Kettering University in 2023. Kenton has led the Kettering EV Kartz competitive electric go kart team for nearly five years and is a multi-faceted automotive enthusiast. His research interests include semi-active suspension design and control, advanced valvetrain motion, battery and battery management systems, power electronics, and EV/HEV powertrains.

Allan R. Taylor received the B.S. and M.S. degrees in electrical engineering from Kettering University, Flint, MI, in 2009 and 2011. From 2011 to 2014, Allan was a Research Assistant within the Advanced Power Electronics Laboratory, Kettering University, working under the direction of Dr. Kevin Bai, focusing on a variety of projects including DC/DC converters and motor drives. Allan worked as a Lecturer at Kettering University from 2014 to 2019 and received a Ph.D. degree in electrical engineering at Michigan State University in 2019. Since 2019, he has been working as an Assistant Professor in the Electrical and Computer Engineering Department at Kettering University. His research interests include power-electronics systems, motor drives, battery-management systems, and alternative energy systems. Allan is an inventor on two industry patents and has co-authored over 20 IEEE journal and conference papers.

Chen Duan is an Assistant Professor in the ECE department at Kettering University, Flint, Michigan, USA. He received the B. S. in Automotive Engineering from University of Science and Technology Beijing, China and M.S. in Automotive Engineering Technology from Kettering University, USA. In 2020, he received the Ph.D. in Electrical Engineering from Wayne State University, USA. From 2013-2022, he worked as a senior engineer on vehicle electrification, automotive electronics and functional safety with FEV North America Inc. Dr. Chen Duan's research interests include hybrid and electric vehicles, power electronics, battery and battery management systems and renewable energy. Dr. Chen Duan has published more than 20 journal and conference papers with IEEE, SAE and IET. Dr. Chen Duan is a certified automotive functional safety professional.